Calcite precipitation dominates the electrical signatures of zero valent iron columns under simulated field conditions

Yuxin Wu[1*], Roelof Versteeg[2], Lee Slater[3] and Douglas LaBrecque[4]

1. *Lawrence Berkeley National Lab,1 Cyclotron Road, Berkeley, Ca 94706, U.S.*
2. *Idaho National Lab, IRC, MS 2025, North Blvd, Idaho Falls, ID 83415, U.S.*
3. *Department of Earth and Environmental Sciences, Rutgers University, 101 warren street, Newark, NJ 07102, U.S..*
4. *Multi-Phase Technologies, 310 Rebecca Dr, Sparks, NV 89436, U. S.*

* Corresponding author: Earth Science Division, Lawrence Berkeley National lab, *MS 90-1116, Berkeley, CA 94720, U.S.*
Tel.: +1 510 486 4793; Fax: +1 510 486 5686
Email address: ywu3@lbl.gov

Abstract

Calcium carbonate is a secondary mineral precipitate influencing zero valent iron (ZVI) barrier reactivity and hydraulic performance. We conducted column experiments to investigate electrical signatures resulting from concurrent $CaCO_3$ and iron oxides precipitation under simulated field geochemical conditions. We identified $CaCO_3$ as a major mineral phase throughout the columns, with magnetite present primarily close to the influent based on XRD analysis. Electrical measurements revealed decreases in conductivity and polarization of both columns, suggesting that electrically insulating $CaCO_3$ dominates the electrical response despite the presence of electrically conductive iron oxides. SEM/EDX imaging suggests that the electrical signal reflects the geometrical arrangement of the mineral phases. $CaCO_3$ forms insulating films on ZVI/magnetite surfaces, restricting charge transfer between the pore electrolyte and ZVI particles, as well as across interconnected ZVI particles. As surface reactivity also depends on the ability of the surface to engage in redox reactions via charge transfer, electrical measurements may provide a minimally invasive technology for monitoring reactivity loss due to $CaCO_3$ precipitation. Comparison between laboratory and field data shows consistent changes in electrical signatures due to iron corrosion and secondary mineral precipitation.

Keywords: ZVI, complex conductivity, polarization, conduction, iron oxides, calcite

1. Introduction

The zero valent iron (ZVI) permeable reactive barrier (PRB) is an *in-situ* technology for the remediation of heavy metals, chlorinated hydrocarbons and radioactive materials in groundwater (Gillham and Ohannesin, 1994; Gu et al., 1998; Su and Puls, 2001; Agrawal et al., 2002). Although encouraging treatment efficiency has been documented (Gu et al., 1998; Morrison et al., 2001; Su and Puls, 2003), reactions between ZVI and groundwater constituents causing ZVI corrosion and subsequent secondary mineral precipitation contribute to long term performance reduction of ZVI PRBs (Liang et al., 2003; Slater and Binley, 2003; Wilkin et al., 2003; Jin Suk et al., 2009). Carbonate minerals (often precipitated concurrent with iron oxides (Mackenzie et al., 1999; Phillips et al., 2000; Liang et al., 2003)), are known to significantly impact ZVI reactivity and hydraulic efficiency in systems with frequently encountered high carbonate groundwater conditions through surface passivation and pore clogging (Agrawal and Tratnyek, 1996; Phillips et al., 2000; Liang et al., 2003; Slater and Binley, 2003; Wilkin et al., 2003; Jeen et al., 2006; Jeen et al., 2007; Jin Suk et al., 2009).

In an anaerobic environment with limited dissolved oxygen (DO) the major iron corrosion reaction is (Furukawa et al., 2002),

$$Fe^0 + 2\ H_2O \rightarrow Fe^{2+} + H_{2(g)} + 2\ OH^- \qquad (1)$$

causing pH increase, decrease of redox potential (Eh) and generation of H_2 gas. Magnetite is a major precipitate during anaerobic corrosion of iron via re-precipitation of dissolved iron and autoreduction of ferric iron on ZVI surfaces (Pryors and Evans, 1950; Bonin et al., 1998). Other than magnetite, calcite is a major mineral phase in systems with high calcium and bicarbonate concentrations through the following reactions (Wolery, 1992),

$HCO_3^- \rightarrow CO_3^{2-} + H^+$ Log K = -10.3 (2)

$H^+ + OH^- \rightarrow H_2O$ Log K = 14 (3)

$Ca^{2+} + CO_3^{2-} \rightarrow CaCO_3$ Log K = -8.3 (4)

with the overall reaction,

$Ca^{2+} + HCO_3^- + OH^- \rightarrow CaCO_{3\,(s)} + H_2O$ Log K = -4.6, (5)

being triggered by the increase of pH (Equation 5).

The dependence of the electrical properties of the iron-electrolyte surface on mineralogy and redox chemistry has motivated studies of the electrical impedance of the iron interface as a function of corrosion. At the micro-scale, Tafel scan and electrochemical impedance spectroscopy (EIS) studies of the ZVI surface during corrosion reactions have identified geochemical controls on ZVI redox reactions (Melitas et al., 2002; Melitas and Farrell, 2002; Mishra and Farrell, 2005). An upscaled, field deployable electrical method, the complex conductivity technique $\sigma^*(\omega)$, has been applied to study ZVI corrosion and mineral precipitation processes in ZVI columns by measuring the frequency dependent electrical properties of the column material (Slater et al., 2005; Wu et al., 2005; Wu et al., 2006).

The measured $\sigma^*(\omega)$ of any porous medium can be represented as,

$$\sigma^*(\omega) = \sigma'(\omega) + i\sigma''(\omega), \quad (6)$$

where ω is the angular frequency, σ' is the measured real part of $\sigma^*(\omega)$, being the conduction (energy loss) component, σ'' is the measured imaginary part of $\sigma^*(\omega)$, being the polarization (energy storage) component and $i = \sqrt{-1}$. At low frequencies (< 1000 Hz), three mechanisms of electrical charge transport can exist in saturated granular ZVI

(Wu et al., 2005). The electrolytic conductivity (σ_{el}) represents conduction occurring via the interconnected, fluid-filled pore space (a purely real term). A complex interfacial conductivity (σ^*_{int}) represents conduction and polarization processes occurring at the iron/electrolyte interface, whereas an electronic conduction term (σ_{elc}) accounts for conduction via interconnected electronically conductive iron minerals. The σ_{el} is linearly dependent on the conductivity of the electrolyte (σ_w) saturating the ZVI column (Archie, 1942) whereas σ^*_{int} incorporates both conduction and polarization within the electrical double layer (EDL) occurring at the electrolyte/iron mineral interface which includes a diffusive mechanism associated with ion migration to and from the metallic surface (Wong, 1979; Slater et al., 2005) and an electrochemical mechanism associated with redox active ions that transfer charge across the mineral/electrolyte interface via redox reactions (Wong, 1979). Whereas measured σ' depends on σ_{el}, σ_{elc} and σ^*_{int}, σ'' is only dependent on σ^*_{int} (i.e. it primarily depends on the interfacial properties of iron minerals).

The reactivity of ZVI is controlled by the number of available reaction sites (i.e. surface area) and the inherent rate of electron transfer between ZVI and the reacting component (Wust et al., 1999; Devlin and Allin, 2005). Electrical methods can be applied to investigate ZVI reactivity changes during corrosion and mineral precipitation processes because electrical methods are sensitive to the amount of available surface area of ZVI (Slater et al., 2005) as well as the rate of charge transfer occurring at the iron/electrolyte interface, i.e. an electrical measurement can potentially be considered some proxy measure of reactivity.

The sensitivity of field deployable electrical methods to ZVI corrosion and mineral precipitation occurring in PRBs has encouraged the use of minimally invasive electrical methods for monitoring barrier ageing (Slater and Binley, 2006). Complex conductivity studies on laboratory ZVI columns (Slater et al., 2005; Wu et al., 2005), as well as field cores extracted from an active PRB (Wu et al., 2006), show that iron oxide precipitation (especially magnetite and green rusts (now called fougerite)) increases the complex conductivity of granular ZVI due to the conductive and polarizable properties of these precipitates (Wu et al., 2005; Wu et al., 2006). However, a recent study showed that calcite precipitation decreases the complex conductivity of granular ZVI due to its non-conductive and redox-inactive properties (Wu et al., 2008).

These previous studies were conducted on laboratory columns with simple geochemical conditions designed to isolate the significance of a certain mineral phase (i.e. iron oxides or calcite) on the electrical responses. Yet PRB precipitate mineralogy is normally complex, being dependent on the groundwater chemistry at the site, in many cases including both iron oxides and calcite (Furukawa et al., 2002; Morrison et al., 2002; Liang et al., 2003; Phillips et al., 2003; Liang et al., 2005). Due to the known contrasting effects of calcite and iron oxides on electrical signatures, studies of systems with both mineral phases are required to further evaluate the potential of electrical measurements as tools for monitoring geochemical changes in PRBs.

Here we report results from column studies designed to simulate the geochemistry of two barriers with high carbonate concentrations, resulting in concurrent $CaCO_3$ and iron oxides precipitation, thereby revealing the electrical signatures likely to result from barrier ageing *in situ*. Our results show that a decrease of both conductivity and

polarization magnitude is observed under ageing processes during concurrent $CaCO_3$ and iron oxides precipitation. An important implication of this work is that $CaCO_3$ appears to exert the dominant role in controlling the electrical properties of corroded iron columns under complex geochemical conditions. In order to evaluate why $CaCO_3$ precipitates appear to dominate the electrical signatures in the presence of mixed $CaCO_3$ and iron oxides we performed a series of SEM imaging of ZVI surfaces and cross sections of ZVI particles. We propose here a mechanism to describe the electrical signatures resulting from parallel $CaCO_3$ and iron oxides precipitation. Our data suggest that the dominant effect of $CaCO_3$ results from the geometrical arrangement of the precipitated mineral phases. The $CaCO_3$ precipitates form an insulating film coating the inner ZVI/magnetite particles, thereby restricting the charge transfer pathway between electrolytic (pore fluid) and electronic (iron metal) conductors causing decreases in electrical conduction and polarization and, presumably, in surface reactivity.

2. Materials and methods

2.1 Site selection

The two study sites selected were the Kansas City, Missouri (KC) site and the east Helena site in Montana. The KC barrier, installed April 1998, was designed to remediate 1,2-dichloroethlene (1,2-DCE) and chloroethene (Wu et al., 2006). The Helena site was constructed in spring 2005 with arsenic being the primary target pollutant (Lien and Wilkin, 2005). The KC barrier was selected as it has a 11 yr operating history with core samples analyzed after eight years of operation (Wu et al., 2006). Helena was selected as it is a new barrier with an electrical resistivity tomography (ERT) monitoring system

installed a year after barrier installation. Both sites exhibit high concentrations of dissolved calcium (1.6mM for Helena, 6.3mM for KC) and bicarbonate (4.4mM for Helena, 5.7mM for KC) expected to promote a precipitate mineralogy including both iron oxides and $CaCO_3$.

2.2 Column setup

Two columns were set up to simulate Helena and KC barrier respectively. Iron material was acquired from Peerless (Detroit, MI), being >90% Fe, 2.5% C, 2.0% Si with trace amounts of Mn and Cr (Su and Puls, 2003). As the surface of this iron is coated by a layer of ferric iron oxides during the manufacturing process, direct exposure of ZVI reaction sites to pore fluid is greatly reduced. A preliminary test showed that, at an accelerated flow rate, fines (mostly > 50 mesh, or <0.3 mm in diameter) were flushed from the column. The ZVI was therefore treated with a quick sieve/wash process to eliminate the majority of the particles finer than 50 mesh.

Columns were transparent polyvinyl chloride (PVC) sample holders (25.5 cm length × 4.8 cm i.d.). Ten electrodes were installed on each column spaced at 1.5 cm intervals, with the first and last electrodes 6 cm away from column ends (Figure 1). Measurement channels were named consecutively from channel 1 (at influent end) to channel 9 (at effluent end). Both the current injection and measurement electrodes were non polarizing electrodes made from silver (Ag) wire coated with silver chloride (AgCl). The current electrodes were wound in a spiral of the same inner diameter as the column so as to facilitate a homogeneous current flow through the columns. The spiral current electrodes installed in both end caps were in direct contact with the sand while the potential electrodes were coupled with the column by suspension in the plastic ports filled with

column saturating electrolytes. The electrodes experienced no observable alterations during the experiment.

The first and last 8.25 cm of each column was packed with Ottawa sand (20-30 mesh in size, no carbonate content according to ASTM tests) to homogenize water flow into and out of the ZVI section occupying the middle 9 cm of the column. We constructed flat sand/iron interfaces perpendicular to the column wall and centered on channel 2 (influent end) and 8 (effluent end). Porosity of the columns (including both granular Fe^0 and sand sections) was calculated to be 45 % by measuring water content in triplicate through weight loss (1% uncertainty).

Helena groundwater contained (all values in mM): K_2SO_4 (0.07), Na_2SO_4 (9), $NaHCO_3$ (4.4), $CaCl_2{\cdot}2H_2O$ (1.6) and $MgCl_2{\cdot}6H_2O$ (0.6) (Lien and Wilkin, 2005). The KC groundwater was prepared based on averaged ground water data collected from multiple upgradient wells (DOE, 2003) and contained (in mM): $NaHCO_3$ (5.7), $CaCl_2$ (6.3), $MgCl_2{\cdot}6H_2O$ (0.75), $MnCl_2{\cdot}4H_2O$ (0.12) and Na_2SO_4 (0.52). The pH of the solutions was adjusted to site specific values at 7.25 ± 0.2 for Helena and 6.7 ± 0.2 for KC columns by adding 6N hydrochloric acid (HCl) drop wise slowly under continuous mixing. To achieve the desired near anaerobic conditions for both sites (DO below 0.1 ppm) solutions were purged with nitrogen gas. Solution containers were then sealed gas tight and a 3-5 psi nitrogen (N_2) flow supplied continuously to the containers, to ensure an anaerobic headspace.

Groundwater seepage velocities are about 0.6 m/day at Helena and 0.1 m/day at the KC site. The columns were designed to simulate 3 and 10 years of operation, over a ~100 day period, for Helena and KC respectively. An accelerated flow rate of 5.3 L/day (6.5

m/day) for Helena and 3 L/day (3.6 m/day) for KC was used. However, columns were terminated earlier (at 88 days for Helena and 80 days for KC) as effluent pHs reached the influent values in both columns, indicating diminishing reactions probably due to surface passivation and/or development of preferential flow paths at high flow rates. The temperature was maintained at 25 ±0.5˚C for the duration of the experiment by placing columns in an environmental chamber. As stressed above, the purpose of these two columns was to simulate late-time reaction processes within a much shorter time frame. We recognize the challenge of replicating field reaction kinetics in column experiments due to the much accelerated flow rates as well as differences in flow pattern, stability of water chemistry, temperature variation, etc. between laboratory and field conditions. However, we hope to capture the major mineralogical phases of interest, i.e. iron oxides and calcite/aragonite, the two dominating phases previously shown to have opposite effects on electrical signatures.

2.3 Geochemical monitoring

Fluid conductivity (σ_w), pH, Eh and dissolved iron were monitored daily. Influent DO was periodically measured to ensure low levels (below 0.1 ppm) consistent with the sites. Solution pH (± 0.1 accuracy) and Eh (± 0.2 mV accuracy) were obtained with an Oakton ion 510 series meter (Vernon Hills, IL) and σ_w with an Oakton pH/CON 300 Meter (±1% accuracy). Dissolved iron was measured with the 1, 10 - phenanthroline titration method (minimum detection limit, MDL = 0.15 ppm) and DO with the Indigo Carmine method (MDL = 0.4 ppm) using commercial photometry test kits (CHEMetrics, Calverton, VA).

2.4 Electrical measurements

A full waveform, multi-channel instrument was used for electrical measurements (Wu et al., 2008). Twelve channels were available for measurements with one designated to a reference resistor (current monitor) and the remainder for the sample channels. Current was injected into the column through spiral electrodes placed in the end caps (Figure 1). Electrical data acquisition was carried out autonomously and automatically.

Electrical measurements were collected over a frequency range from 0.01 – 1000 Hz with a constant voltage (1 V) applied across the spiral electrodes at the selected frequency, and resulting full waveform voltages measured over both reference resistor and measurement channels. Digitized waveforms were stored in a relational database and the conductivity amplitude ($|\sigma|$) and phase shift (ϕ) calculated for each channel through an iterative waveform misfit fitting procedure (Versteeg et al., 2006). This procedure has an error of about 1 % for $|\sigma|$, and about 0.2 mrad for ϕ. The real (σ'') and imaginary (σ') parts of the complex conductivity were calculated from,

$$\sigma'' = |\sigma| \times \sin\phi, \tag{7}$$

$$\sigma' = |\sigma| \times \cos\phi. \tag{8}$$

2.5 Electrical data modeling

Macroscopic phenomenological models, such as the Cole-Cole model (Pelton, 1978), are typically adopted to describe $\sigma^*(\omega)$ of soils (see for review (Dias, 2000)) as physics-based models are lacking. In the Cole-Cole model, the frequency (ω) dependence of σ^* is modeled as (Jones, 2002),

$$\sigma^*(\omega) = \sigma_0 \left[1 + m \left(\frac{(i\omega\tau)^c}{1 + (i\omega\tau)^c (1-m)} \right) \right] \tag{9}$$

where σ_0 is the conductivity at DC frequency, τ is the mean relaxation time, c is a shape exponent (typically 0.1-0.6) and m is the chargeability, a measure of the polarization magnitude, ($m = 1-\sigma_0/\sigma_\infty$, where σ_∞ is the conductivity at high frequency). The two model parameters of most interest here are σ_0 and $m_n = m \times \sigma_0$, representing global measures of conductivity and interfacial polarization magnitude, respectively (Lesmes and Frye, 2001). We inverted the electrical data using a deterministic algorithm based on a least-squares approach with Marquardt regularization (Kemna, 2000). Although this inversion method offers reasonable parameter estimates satisfying the purpose of this study, recently developed stochastic inversion algorithms (using a Bayesian framework) have shown improved parameter estimates and tighter uncertainty bounds of parameters (Ghorbani et al., 2007; Chen et al., 2008).

2.6 Solid phase analysis

Columns were transported into an anaerobic chamber (95:5 N_2 to H_2 volume ratio) to extract samples for solid phase characterization after completion of the experiment. One sample was acquired from each iron bearing channel of both columns (black dots in Figure 1) and split into two sub-samples for scanning electron microscopy (SEM) imaging and X-ray diffractometry (XRD) analysis. Samples were washed with deoxygenated acetone/deionized water solution (1:1 volume ratio) to prevent residuals from precipitation during drying and then left to dry in the chamber. Surface and cross sectional SEM imaging of multiple particles was performed to characterize morphological and mineralogical changes resulting from corrosion and precipitation in each column. A LEO 1530 VP field emission SEM equipped with energy dispersive X-ray spectroscopy (EDX) was used for image acquisition and elemental analysis. Surface

imaging was carried out on dried samples directly extracted from the anaerobic chamber without further treatment to minimize contamination. For cross sectional imaging, five grams of sample from each channel were impregnated into epoxy resin (7:3 resin/hardener ratio by volume) in the anaerobic chamber. Impregnated samples were then subject to a vacuum oven at 60 ºC for 20 hours. After curing, samples were polished to acquire a cross section of iron particles. A layer of Au/Pd (several angstroms in thickness) was coated onto the polished surface to facilitate electronic conduction and prevent surface charging before SEM analysis.

XRD, assisted by SEM/EDX imaging, was the major tool used for mineral phase identification. Approximately 50 grams of each sample were ground to acquire fine grains. A Philips PW3040 powder XRD was employed following procedures described elsewhere (Wu et al., 2005).

3. Results

3.1 Fluid geochemistry

We plot all temporal experimental data against volume of solution flushed through the column (as opposed to experimental time) in order to facilitate comparison between the columns at different flow rates. Note that the total solution volumes used for the Helena and KC columns were 460 L and 250 L respectively. The pH of Helena column increased from 7.25 ± 0.3 to 8.2 ± 0.2 after passing through the column and remained steady for the first 220 L of solution, being followed by a period of gradual decrease back to 7.4 ± 0.1 for the last 240 L of solution (Figure 2a). For the KC column, the pH increased from 6.7 ± 0.3 to 7.2 ± 0.2 after passing through the column for the first 120 L of solution

followed by a period of gradual decrease back to 6.7 ± 0.1 for the last 120 L of solution. Available field data show that the pH inside the KC barrier is between 9~10 (Wu et al., 2006), being higher than what we observed here in the laboratory. This is likely due to the much higher flow rates in the column experiments resulting in much shorter residence times and therefore less time for reactions to occur.

The Helena column Eh dropped from -37 mV to between -85 and -90 mV during flushing with the first 220 L of solution (Figure 2b). Similar to pH, the Eh gradually recovered back to around -42 mV (close to the influent value) subsequent to flushing with the last 220 L of solution. For the KC column, the effluent Eh dropped to and stayed steady between -25 and -30 mV compared to about -4 mV at the influent during the first 120 L of solution. After that, the Eh gradually climbed back to about – 5 mV, almost the same as the influent Eh at the end of the experiment with a total of about 240 L of solution used for this column. The Eh values observed in this lab column experiment were higher than those observed in the field at the KC site (~200mV) (Wu et al., 2006) further indicating differences in reaction kinetics probably due to differences in flow rates. Effluent fluid conductivity changes were minimal for both columns with 6% and 5% variation for Helena and KC columns, respectively (Figure 2c). Effluent pH and Eh (the two indicators of redox reactions) of the two columns both experienced initial increases followed by a gradual recovery back to influent values indicating reactivity loss towards the end of the experiment. This reactivity loss is probably due to a passivation effect and/or development of preferential flow path at high flow rates. Despite the initial higher values, ferrous iron concentrations were relatively stable at ~1 and ~0.2 ppm for

Helena and KC respectively, indicating a moderately reducing condition in the column (Figure 2d).

3.2 Solid phase analysis

Typical morphologies of the mineralogy phases identified from solid phase sampling and imaging as well as XRD results from the Helena column are presented in Figure 3 and 4. Note that the KC column has similar XRD mineralogy profiles (data not shown for brevity). The solid phase analysis identified major mineral phases as being calcite, aragonite and magnetite with clear similarities between the two columns.

However, based on electrochemical modeling results using PHREEQC (USGS), other potential mineral precipitates could include ferrihydrite, goethite, lepidocrocite, maghemite and siderite (Saturation indices (SI) listed in table 1). As only limited characterization and geochemical data were collected during the experiment the modeling was carried out based primarily on the initial solution geochemistry and the ZVI material characteristics. Furthermore, as the high flow rate may have prevented the in column reactions from reaching equilibrium, the modeling was carried out step wised with a limited amount of reactive species supplied from the solid (1 mM of Fe^0 and hematite respectively) in each step. The pH data from the columns was used to locate the particular step in this series of reaction steps best matching the column conditions. Fe^0 and hematite were considered the major solid-phase reactive species as hematite is the outermost layer of the ZVI grains and Fe^0 is the major electron donor. We note that this modeling is limited as the model carried the reactions to equilibrium whenever possible within each step, which is not necessarily the case for the columns.

Although more phases (including siderite and other forms of iron oxides) were at super-saturation based on modeling results (Table 1), characteristic peaks for these phases were not identified in the XRD spectrum, suggesting either limited concentrations or a sporadic existence. The XRD results for Helena show magnetite peaks (at 2θ = 30.1˚, 35.45˚, 57˚ and 62.5˚) are present predominantly at the first 2-3 channels (Channels 2, 3 and 4) closest to the influent, whereas peaks are reduced deeper into the column (Channels 5-8). Figure 3a shows an example of poorly crystallized magnetite precipitation extracted from channel 2 of Helena column with EDX analysis revealing O and Fe as the major elements with a Fe/O atomic ratio of ~3:4, excluding the amount of O in coordination with Ca assuming a 1:3 O/Ca ratio (calcite/aragonite). Similar to magnetite, calcite is also a mineral phase primarily present at the first 2-3 channels of each column as demonstrated from the XRD spectrum (Figure 4, major peak at 2θ = 29.5˚). Figure 3d shows an example of well crystallized rhombohedron calcite crystals with EDX analysis showing C, O and Ca as major elemental compositions. Unlike calcite, which only dominates at the channels close to influent, aragonite is a dominant phase in all iron-containing channels of each column as demonstrated by XRD analysis (Figure 4). Figure 3b, c demonstrate the major morphologies of calcium carbonate (probably aragonite based on characteristic crystal shapes) accompanied by EDX elemental analysis. Figure 3b shows needle shaped aragonite with mixed iron oxide precipitation. Figure 3c shows a well crystallized rod shaped aragonite crystal with EDX analysis confirming the major elemental composition of C, O and Ca. Fougerite was interpreted as sporadically present as a minor phase based on its characteristic hexagonal crystal shape identified in images (Figure not shown). However, XRD analysis did not

identify fougerite peaks (similar to other phases) possibly indicating a low concentration and/or sporadic existence. Iron columns saturated with high carbonate solutions have previously shown precipitation of iron hydroxy carbonate (Jeen et al., 2007; Jeen et al., 2008). However, this mineral phase was not identified in our experiment which could possibly be attributed to the differences in flow rates and solution complexity, both influencing reaction kinetics and mineralogy (Gui and Devine, 1995; Farrell et al., 2000).

Cross sectional SEM imaging revealed corrosion rinds coating ZVI cores with a typical thickness ranging from a few to over 100 μm. Figure 5 shows an example of a cross sectional SEM image with EDX analysis revealing the profile of elemental compositions across the corrosion rind. At the inner core of the corroded iron particle (Figure 5a) Fe is the only major element present, confirming unaltered iron core. At the inner part of the corrosion rind (Figure 5b), the major elements identified are C, O, Fe and Ca, indicating the mixed coexistence of iron oxides (possibly magnetite) and $CaCO_3$ with similar peak heights for Fe and Ca and an Fe/Ca atomic ratio of 7:5. The elemental composition at the outer layer of the corrosion rind is the same as the inner layer. However, the Fe peak height is much smaller relative to Ca, and the Fe/Ca atomic ratio at this location is less than 1:2 (Figure 5c). Although it is difficult to make quantitative estimates, the differences in peak heights and atomic ratios indicate a much higher Ca concentration at the outer portion of the corrosion rind relative to the inner portion. This elemental composition pattern was observed in most of the grains imaged, with images from other locations in the columns shown in Figure 6. This observation is significant as it suggests the dominance of $CaCO_3$ precipitation on the outer layer of the corrosion rinds that we

believe effectively acts an electrical insulator coating the iron particles and explains our electrical signatures.

3.3 Electrical data

Time lapse σ' and σ" as well as model parameters (σ_0 and m_n) exhibits a consistent and significant decrease over the experiment duration at the interface channels (channel 2) of both columns, with a much greater rate of change early in the experiment (Figure 7). The difference in the background electrical data is caused by the difference in the fluid conductivity of the two solutions. Similar to the interface channels, channels deeper within the columns demonstrate the same trend for both σ' and σ" (data not shown) indicating a consistent response of the whole column to the reaction processes. Figure 7e and 7f show Cole-Cole modeling results consistent with the spectral σ' and σ" data with a continuous decrease of DC conductivity (σ_0) and polarization magnitude (m_n). Figure 7e shows decreases of σ_0 for both columns with an overall decrease of 63% for Helena and 76% for KC columns. Figure 7f reveals decreases of m_n with approximately 79% decrease for Helena and 77% for KC columns. The channels deeper in the columns show similar changes to those for the interface channels (data not shown). Table 2 summarizes the percentage decreases in σ_0 and m_n for all iron-bearing channels of both columns.

4. Discussion

Solid phase analysis showed that magnetite and $CaCO_3$ (including both calcite and aragonite) are the two major phases under the conditions simulated in this study. Magnetite and calcite dominate close to the influent, with aragonite becoming dominant deeper within the columns.

Based on Table 1, mineral phases predicted from modeling but not developed in the laboratory columns include siderite, sulfide minerals as well as other forms of iron oxides. The absence of sulfide minerals can be attributed to lack of microbial activity due to the short experimental duration. Magnetite has the highest SI among all the oxides species which likely caused the dominancy of magnetite among the oxide species observed in the columns. As a result of the concentrations of Ca being two orders of magnitude higher than that of dissolved iron, calcium carbonate (calcite and aragonite) will likely precipitate as the major carbonate species although saturation indices are smaller than for siderite. Interestingly, the potential precipitate phases modeled with PHREEQC are a closer match to the mineralogical profile developed under field conditions based on core analysis (Wu, et al., 2006). This suggests that differences in reaction kinetics caused by the much higher flow rates may explain the absence of potential phases identified from modeling in the columns. This discrepancy in precipitate phases between modeling and laboratory measurements reflects the limited ability of the accelerated flow column experiment to fully replicate field conditions. However, although the full spectrum of potential mineral phases was not reproduced in these columns, the major mineral phases of concern (magnetite and calcite/aragonite) were captured.

Considering the geochemical data and solid phase analysis, we propose here a conceptual reaction model that could explain the observed electrical data. In our columns, the limiting factors for magnetite precipitation under limited DO conditions are primarily pH and the availability of iron/electrolyte contact surface area whereas the limiting factors for $CaCO_3$ precipitation are pH and reactant concentrations, i.e. calcium and

carbonate controlling saturation level. At the channels close to the influent end, the anaerobic corrosion of iron occurs due to the low DO of the solution and results in magnetite precipitation, accompanied by pH increase, according to equation 1. As noted previously, the pH increase observed is much less than in previous laboratory and field studies due probably to the higher flow rate used as well as the buffering effect of the carbonate/bicarbonate couple. Based on the simulations elevated pH at these channels caused oversaturation and the subsequent precipitation of $CaCO_3$ (for calcite, K_{sp}=4.96 × 10^{-9}). The precipitation of iron oxides and electrically insulating $CaCO_3$ on ZVI surfaces reduces the iron/electrolyte contact surface area, thereby inhibiting further precipitation of iron oxides and reducing iron reactivity and corrosion rates over time. The reduction of iron reactivity due to calcite precipitation was investigated in a recent study using DCE as the target contaminant (Jin Suk et al., 2009). These studies show that iron reactivity loss due to significant surface passivation as well as loss of porosity by calcite precipitation under high corrosion rate reduces the efficiency of PRBs in remediating target contaminants. A direct comparison of calcite precipitation and subsequent reactivity loss between our laboratory study and available field data at the KC barrier is not feasible as the laboratory experiment did not target contaminants.

As mentioned in the results, we also observed that calcite exists predominantly in the first 2-3 channels closest to the influent interface while aragonite exists in all the channels. Available geochemical data does not provide enough information for further investigation of this observation. However, we tentatively attribute this to a inhibition of calcite crystal growth by dissolved ferrous iron presumably present at higher concentrations in the deeper channels (Wada et al., 1995).

Previous research has demonstrated that mineralogy is a critical factor controlling the electrical signatures resulting from iron corrosion and mineral precipitation in ZVI PRBs (Wu et al., 2008). In previous comparative studies of the electrical signatures from magnetite/fougerite vs. calcite precipitation it was shown that, in contrast to the increase of electrical conductivity and polarization due to magnetite/fougerite precipitation, calcite precipitation decreases the electrical conductivity and polarization. This was predominantly attributed to the contrasting electrical properties of the different mineralogies: i.e. conductive and polarizable magnetite/fougerite vs. non conductive and non polarizable calcite (Wu et al., 2008).

In contrast to previous column studies which were conducted under simple electrolyte conditions, our parallel studies of two columns saturated with simulated site groundwater resulted in a more complex mineralogy profile being a closer approximation to real field conditions. As discussed above, although available field data have shown a more complex mineralogical profile than what was observed in this experiment, we successfully captured the two major mineral phases (iron oxides and calcite) that are most significant with respect to electrical signatures. We thus consider the data shown here to be the first approximation of the likely electrical signatures in active field PRB installations when the groundwater chemistry is susceptible to $CaCO_3$ precipitation.

Time lapse geophysical data collected from the Helena site starting from a year after barrier installation have revealed increases of resistivity (decreases of conductivity) at the lower part of the barrier where groundwater flow rate is high, consistent with our column studies (Figure 8), although the upper part of the barrier shows opposite changes with

respect to conductivity (polarization still deceases consistent with laboratory results) that warrant further investigation.

Our observation of significant decrease of conductivity and polarization magnitude suggests that, in a system with both iron oxides and $CaCO_3$ (calcite or aragonite) being dominant phases, $CaCO_3$ precipitation plays the dominant role in controlling the changes of electrical signatures. A significant finding of this study is the impact of the geometry of the competing (in terms of electrical properties) primary mineral phases within the system. Based on the proposed conceptual reaction model, supported by the cross-sectional SEM imaging of the solid phase (Figure 5 and 6), we suggest that the $CaCO_3$ precipitate exerts the dominant control on the electrical signatures when it precipitates at the outer portion of the corroded iron surface, producing an electrically insulating film in contact with electrolyte. The fact that calcite precipitation results in a concurrent decrease in electrical signatures and iron reactivity suggests the potential of using electrical signals as proxy indicators of reactivity. However, to establish a firm link between electrical signals and reactivity change, further investigations are needed to investigate (1) the relationship between the electrical signals and the rate of charge transfer across the mineral/electrolyte interface, another factor controlling reactivity and (2) the link between electrical signals and reactivity in the presence of target contaminants during active remediation.

Field application of electrical methods should clearly consider the effect of the contaminants. The effect of contaminant reactions on electrical signatures has not been investigated. However, we anticipate this effect will be minor because of typically small concentrations of contaminants, i.e. small contribution to the overall

corrosion/precipitation processes relative to natural groundwater constituents However, it is possible that contaminants could cause significant electrode alterations, by coating electrode surfaces or causing electrode corrosion. A study of such effect is ultimately needed.

5. Conclusion

The electrical behavior, especially the polarization component, of granular ZVI material is closely associated with the iron/electrolyte interface because the charge transfer is through tangential movement of charged ions along this interface as well as redox reactions involving electron transfer across it. The alteration of this interface with regard to its charge transfer properties significantly changes its electrical conduction behavior. Because we observed significant reduction of both electrical conductivity and polarization magnitude, we assume a reduction in charge transfer at the iron/electrolyte interface that we attribute to the geometrical arrangement of the precipitate mineral phases. As revealed from EDX analysis of the SEM images, $CaCO_3$ precipitation tends to form a mixture with iron minerals, which significantly reduces the conductivity and polarizability of the material. Importantly, based on EDX analyses of corrosion rinds, $CaCO_3$ precipitation tends to form an outer layer covering iron oxide precipitates which acts as a nonconductive passive film and causes significant loss of electrical conduction and polarization of the particles, thus causing significant decrease of the bulk conductivity and polarization magnitude of the material.

The changes of both electrical properties and reactivity of ZVI are strongly related to the tendency for redox reactions to occur at the iron/electrolyte interface. Therefore, the redox reactions occurring at the iron/electrolyte interface likely cause parallel changes of

both electrical properties and redox reactivity of the material. Although further investigation is needed, we suggest that the electrical properties can possibly be used as an indirect proxy measure of iron reactivity in the presence of $CaCO_3$ precipitation through the sensitivity to changes of ZVI surface properties. In this study we suggest a decreased reactivity of the ZVI material based on the observed decrease of electrical signatures due to the precipitation of $CaCO_3$ as an insulating film on the iron particles. Comparison between laboratory and field data shows some consistency with respect to electrical signatures and precipitate mineralogy. However, it appears that flow rate is a critical factor controlling the reaction kinetics, rendering it difficult to simulate long term corrosion/precipitation processes in columns using accelerated flow rates Electrical measurements could be developed for evaluating changes of iron reactivity due to redox-related surface reactions within active ZVI PRB installations where groundwater conditions promote $CaCO_3$ precipitation.

Acknowledgements

This research was supported by the DOE contract DE-FG-02-04ER84013 (P.I. Douglas LaBrecque) from Office of Small Business Innovation Research (SBIR). This work was also partially supported by the U.S. Department of Energy under Contract No. DE-AC02-05CH11231. The CR system was supported by Idaho National Laboratory (INL) Laboratory Directed Research and Development (LDRD) funding. We thank Andreas Kemna (University of Bonn) for use of a Cole Cole relaxation modeling code and Nic Spycher (LBNL) for help with geochemical modeling. We also acknowledge the editor and two reviewers for constructive comments that improved the manuscript.

Literature Cited

Agrawal, A. et al., 2002. Effects of carbonate species on the kinetics of dechlorination of 1,1,1-trichloroethane by zero-valent iron. Environmental Science & Technology, 36(20): 4326-4333.

Agrawal, A. and Tratnyek, P.G., 1996. Reduction of nitro aromatic compounds by zero-valent iron metal. Environmental Science & Technology, 30(1): 153-160.

Archie, G.E., 1942. The electrical resistivity log as an aid in determining some reservoir characteristics: Transactions of the American Institute of Mineral. Metallurgy and Petroleum Engineers, 146: 54-62.

Bonin, P.M.L., Odziemkowski, M.S. and Gillham, R.W., 1998. Influence of chlorinated solvents on polarization and corrosion behavior of iron in borate buffer. Corrosion Science, 40(8): 1391-1409.

Chen, J., Kemna, A. and Hubbard, S., 2008. A comparison between Gauss-Newton and Markov chain Monte Carlo based methods for inverting spectral induced polarization data for Cole-Cole parameters. Geophysics, 73(6): F247-F259.

Devlin, J.F. and Allin, K.O., 2005. Major anion effects on the kinetics and reactivity of granular iron in glass-encased magnet batch reactor experiments. Environmental Science & Technology, 39(6): 1868-1874.

Dias, C., 2000. Developments in a model to describe low-frequency electrical polarization in rocks. Geophysics, 65: 437-451.

DOE, 2003. Annual Groundwater Corrective Action Report Volume 1, United States Department of Energy (DOE), Kansas City Office, Honeywell Federal Manufacturing & Technologies, Kansas City, Missouri.

Farrell, J., Kason, M., Melitas, N. and Li, T., 2000. Investigation of the long-term performance of zero-valent iron for reductive dechlorination of trichloroethylene. Environmental Science & Technology, 34(3): 514-521.

Furukawa, Y., Kim, J.W., Watkins, J. and Wilkin, R.T., 2002. Formation of ferrihydrite and associated iron corrosion products in permeable reactive barriers of zero-valent iron. Environmental Science & Technology, 36(24): 5469-5475.

Ghorbani, A., Camerlynck, C., Florsch, N., Cosenza, P. and Revil, A., 2007. Bayesian inference of the Cole-Cole parameters from time- and frequency-domain induced polarization. Geophysical prospecting, 55(4): 589-605.

Gillham, R.W. and Ohannesin, S.F., 1994. Enhanced Degradation of Halogenated Aliphatics by Zero-Valent Iron. Ground Water, 32(6): 958-967.

Gu, B., Liang, L., Dickey, M.J., Yin, X. and Dai, S., 1998. Reductive precipitation of uranium(VI) by zero-valent iron. Environmental Science & Technology, 32(21): 3366-3373.

Gui, J. and Devine, T.M., 1995. A Sers investigation of the passive films formed on iron in mildly alkaline solutions of carboante/bicarboante and nitrate. Corrosion Science, 37(8): 1177-1189.

Jeen, S.-W., Blowes, D.W. and Gillham, R.W., 2008. Performance evaluation of graunlar iron for removing hexavalent chromium under different geochemical conditions. Journal of Contaminant Hydrology, 95: 76-91.

Jeen, S.-W., Gillham, R.W. and Blowes, D.W., 2006. Effects of carbonate precipitates on long-term performance of granular iron for reductive dechlorination of TCE. Environmental Science & Technology, 40(20): 6432-6437.

Jeen, S.-W., Jambor, J.L., Blowes, D.W. and Gillham, R.W., 2007. Precipitates on Granular Iron in Solutions Containing Calcium Carbonate with Trichloroethene and Hexvalent Chromium. Environmental Science & Technology, 41: 1989-1994.

Jin Suk, O., Jeen, S.-W., Gillham, R.W. and Gui, L., 2009. Effects of initial iron corrosion rate on long-term performance of iron permeable reactive barriers: Column experiments and numerical simulation. Journal of contaminant Hydrology, 103: 145-156.

Jones, D.P., 2002. Investigation of clay-organic reactions using complex resistivity. MS thesis Thesis, Colorado School of Mines, 403 pp.

Kemna, A., 2000. Tomographic inversion of complex resistivity - theory and application. Der Andere Verlag, Osnabrück, Germany.

Lesmes, D.P. and Frye, K.M., 2001. Influence of pore fluid chemistry on the complex conductivity and induced polarization responses of Berea sandstone. Journal of Geophysical Research-Solid Earth, 106(B3): 4079-4090.

Liang, L., Moline, G.R., Kamolpornwijit, W. and West, O.R., 2005. Influence of hydrogeochemical processes on zero-valent iron reactive barrier performance: A field investigation. Journal of Contaminant Hydrology, 78: 291-312.

Liang, L.Y., Sullivan, A.B., West, O.R., Moline, G.R. and Kamolpornwijit, W., 2003. Predicting the precipitation of mineral phases in permeable reactive barriers. Environmental Engineering Science, 20(6): 635-653.

Lien, H.L. and Wilkin, R.T., 2005. High-level arsenite removal from groundwater by zero-valent iron. Chemosphere, 59(33): 377-386.

Mackenzie, P.D., Horney, D.P. and Sivavec, T.M., 1999. Mineral precipitation and porosity losses in granular iron columns. Journal of Hazardous Materials, 68(1-2): 1-17.

Melitas, N., Conklin, M. and Farrell, J., 2002. Electrochemical Study of Arsenate and Water Reduction on Iron Media Used for Arsenic Removal from Potable Water. Environmental Science & Technology, 36: 3188-3193.

Melitas, N. and Farrell, J., 2002. Understanding Chromate reaction kinetics with corroding iron media using Tafel analysis and Electrochemical Impedance Spectroscopy. Environmental Science & Technology, 36: 5476-5482.

Mishra, D. and Farrell, J., 2005. Understanding nitrate reactions with zerovalent iron using tafel analysis and electrochemical impedance spectroscopy. Environmental Science & Technology, 39(2): 645-650.

Morrison, S.J., Metzler, D.R. and Carpenter, C.E., 2001. Uranium precipitation in a permeable reactive barrier by progressive irreversible dissolution of zerovalent iron. Environmental Science & Technology, 35(2): 385-390.

Morrison, S.J., Metzler, D.R. and Dwyer, B.P., 2002. Removal of As, Mn, Mo, Se, U, V and Zn from groundwater by zero-valent iron in a passive treatment cell: reaction progress modeling. Journal of Contaminant Hydrology, 56(1-2): 99-116.

Pelton, W.H., Sill, W.R., Smith, B.D., 1978. Interpretation of complex resistivity and dielectric data. Part I. Geophysical Transactions, 29: 297-330.

Phillips, D.H. et al., 2000. Performance evaluation of a zerovalent iron reactive barrier: Mineralogical characteristics. Environmental Science & Technology, 34(19): 4169-4176.

Phillips, D.H., Watson, D.B., Roh, Y. and Gu, B., 2003. Mineralogical characteristics and transformations during long-term operation of a zerovalent iron reactive barrier. Journal of Environmental Quality, 32(6): 2033-2045.

Pryors, M.J. and Evans, U.R., 1950. Chemical communication. J. Am. Chem. Soc.: 1259.

Slater, L. and Binley, A., 2003. Evaluation of permeable reactive barrier (PRB) integrity using electrical imaging methods. Geophysics, 68(3): 911-921.

Slater, L. and Binley, A., 2006. Engineered barriers for pollutant containment and remediation. In: H. Vereecken, A. Binley, G. Cassiani, A. Revil and K. Titov (Editors), Applied Hydrogeophysics. Springer, pp. 293-317.

Slater, L.D., Choi, J. and Wu, Y., 2005. Electrical properties of iron-sand columns: Implications for induced polarization investigation and performance monitoring of iron-wall barriers. Geophysics, 70(4): G87-G94.

Su, C.M. and Puls, R.W., 2001. Arsenate and arsenite removal by zerovalent iron: Kinetics, redox transformation, and implications for in situ groundwater remediation. Environmental Science & Technology, 35(7): 1487-1492.

Su, C.M. and Puls, R.W., 2003. In situ remediation of arsenic in simulated groundwater using zerovalent iron: Laboratory column tests on combined effects of phosphate and silicate. Environmental Science & Technology, 37(11): 2582-2587.

Versteeg, R. et al., 2006. Automated acquisition and processing of multichannel complex resistivity data, SAGEEP, Bellevue,WA.

Wada, N., Yamashita, K. and Umegaki, T., 1995. Effects of divalent cations upon nucleation, growth and transformation of calcium carbonate polymorphs under conditions of double diffusion. Journal of Crystal Growth, 148: 297-304.

Wilkin, R.T., Puls, R.W. and Sewell, G.W., 2003. Long-term performance of permeable reactive barriers using zero-valent iron: Geochemical and microbiological effects. Ground Water, 41(4): 493-503.

Wolery, T.J., 1992. EQ3/6, a software package for geochemical modeling of aqueous systems, Lawrence Livermore National Laboratory, Berkeley, CA.

Wong, J., 1979. An electrochemical model of the induced-polarization phenomenon in disseminated sulfide ores. Geophysics, 44: 1245-1265.

Wu, Y., Slater, L., Versteeg, R. and LaBrecque, D., 2008. A comparison of the low frequency electrical signatures of iron oxide versus calcite precipitation in granular zero valent iron columns. Journal of Contaminant Hydrology, 95(3-4): 154-167.

Wu, Y., Slater, L.D. and Korte, N., 2005. Effect of precipitation on low frequency electrical properties of zero valent iron columns. Environmental Science & Technology, 39: 9197-9204.

Wu, Y., Slater, L.D. and Korte, N., 2006. Low Frequency Electrical Properties of Corroded Iron Barrier Cores. Environmental Science & Technology, 40: 2254-2261.

Wust, W.F., Kober, R., Schlicker, O. and Dahmke, A., 1999. Combined zero- and first-order kinetic model of the degradation of TCE and *cis*-DCE with commercial iron. Environment Science and Technology, 33(23): 4304-4309.

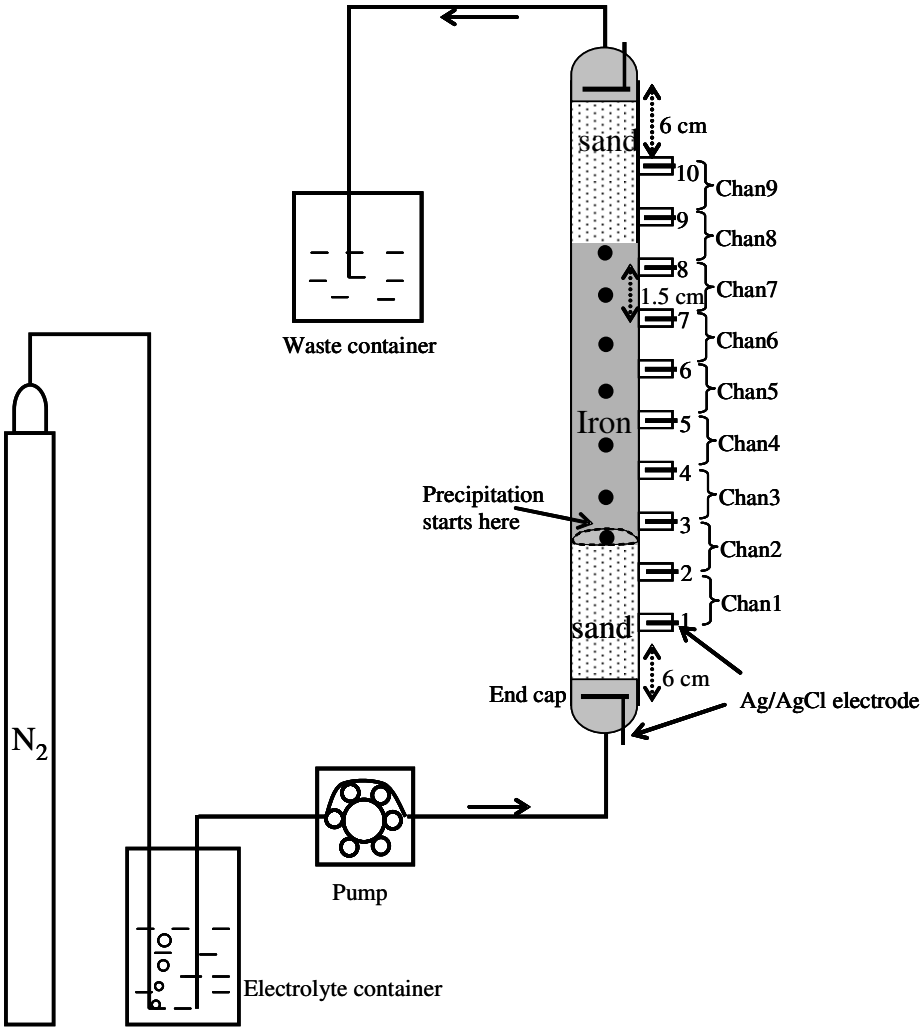

Figure 1. Schematic diagram of the column setup showing column and channel configuration as well as the method of anaerobic control. Note that the black dots represent the sampling locations during destructive solid phase analysis after column termination.

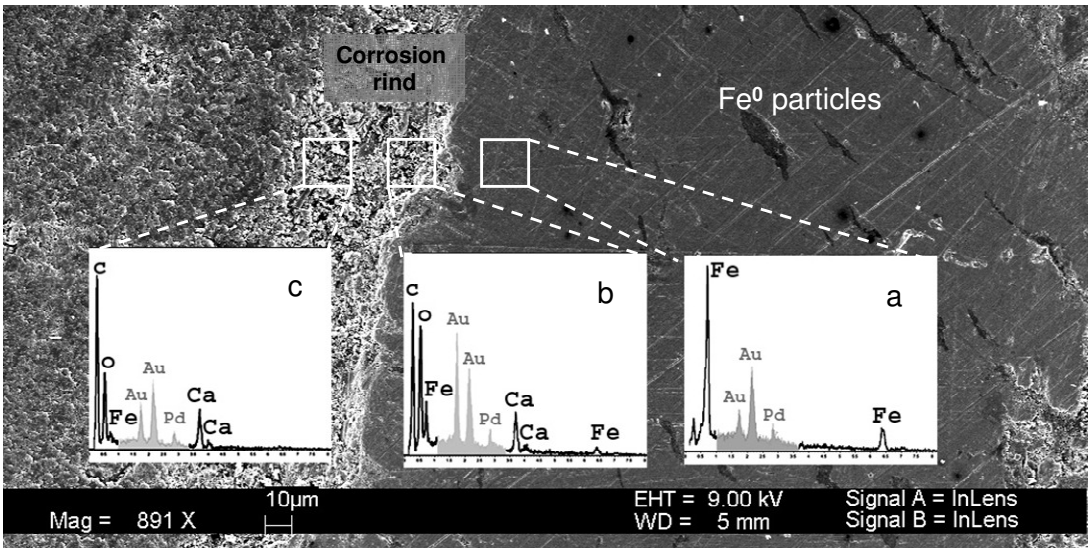

Figure 2. Effluent chemistry of Helena (●) and KC (○) columns with influent chemistry plotted at volume 0 for comparison: (a) pH; (b) Eh; (c) σ_w and (d) Dissolved iron.

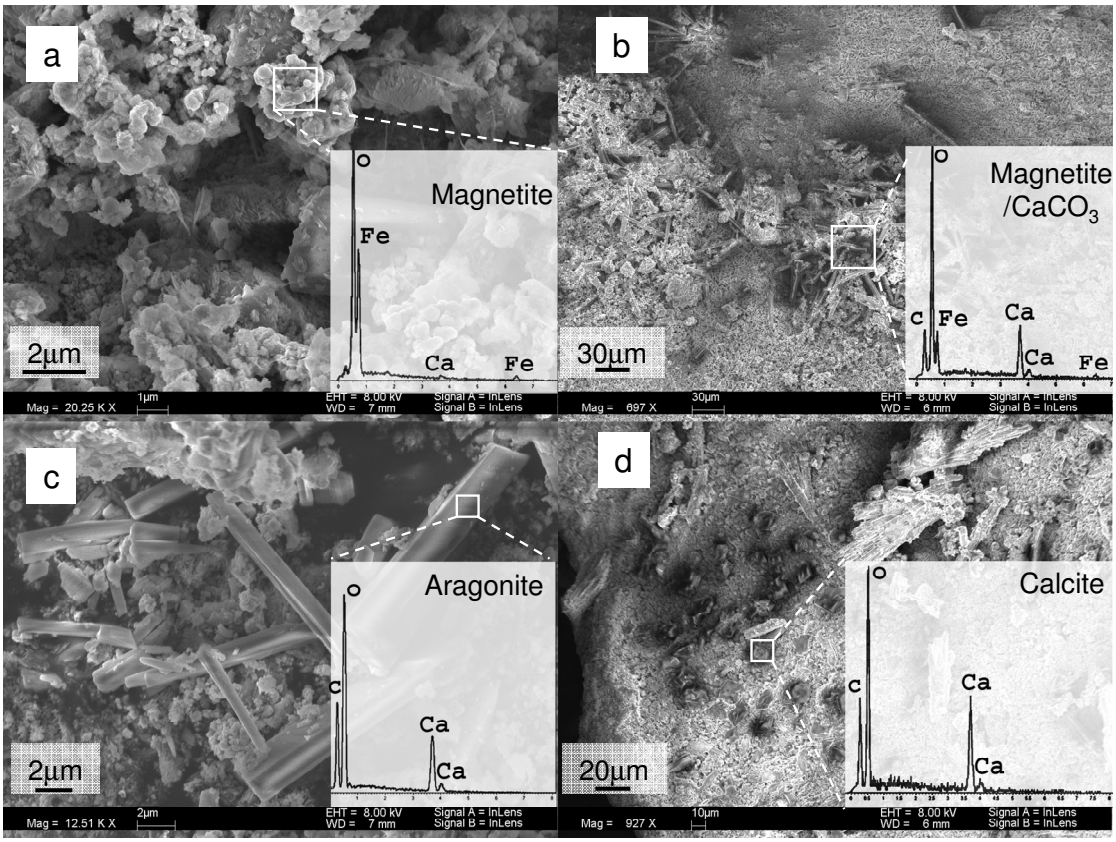

Figure 3. Surface images of major mineralogy and crystal morphology identified from the columns with EDX elemental analysis on selected area.

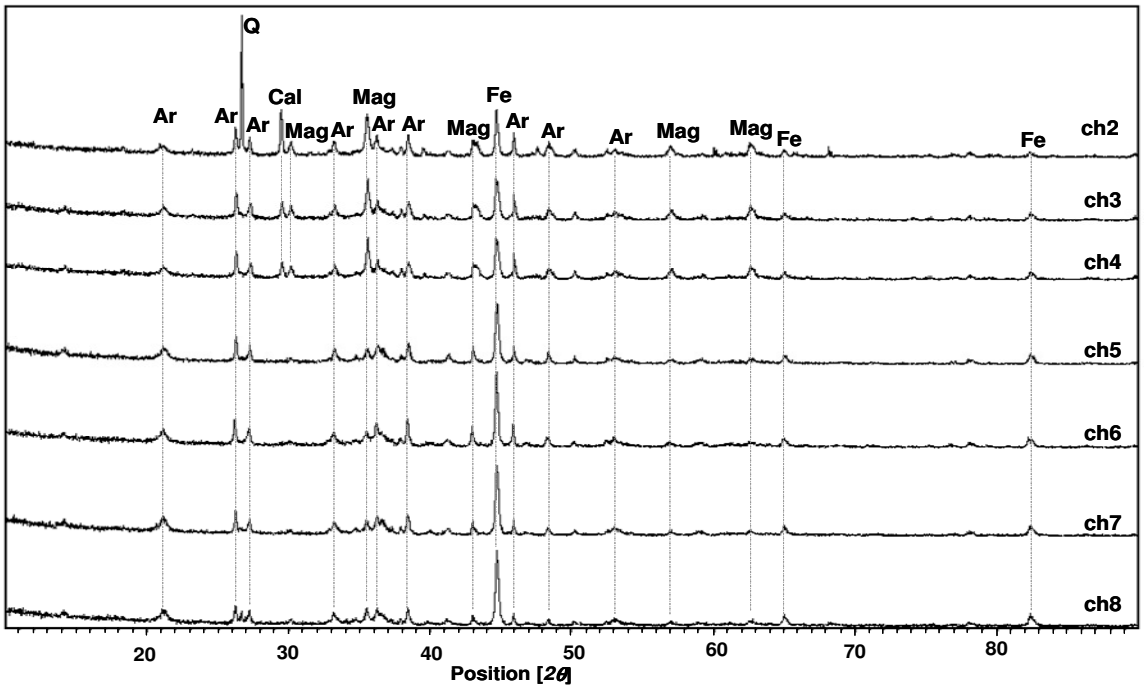

Figure 4. X-ray diffractograms of samples extracted from Helena column. Ar- aragonite, Cal – calcite, Mag – magnetite, Fe – ZVI, Q – quartz. Quartz is identified at channel 2 due to the sand pack towards the end of the columns.

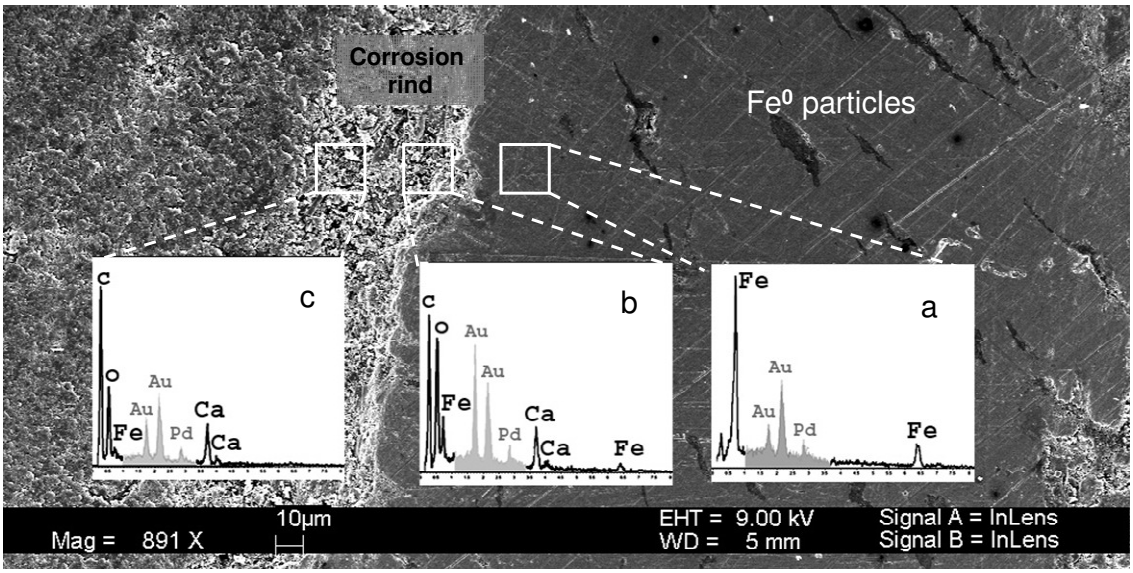

Figure 5. Cross sectional SEM image showing corrosion rind of an iron particle. EDX analyses of specific locations are shown to demonstrate the change of elemental composition in the cross section: (a) at the inner ZVI core; (b) at the inner part of corrosion rind and (c) at the outer part of the corrosion rind. Note that the peaks from Au/Pd surface coating during sample preparation are made grey as they are background noise introduced during sample preparation.

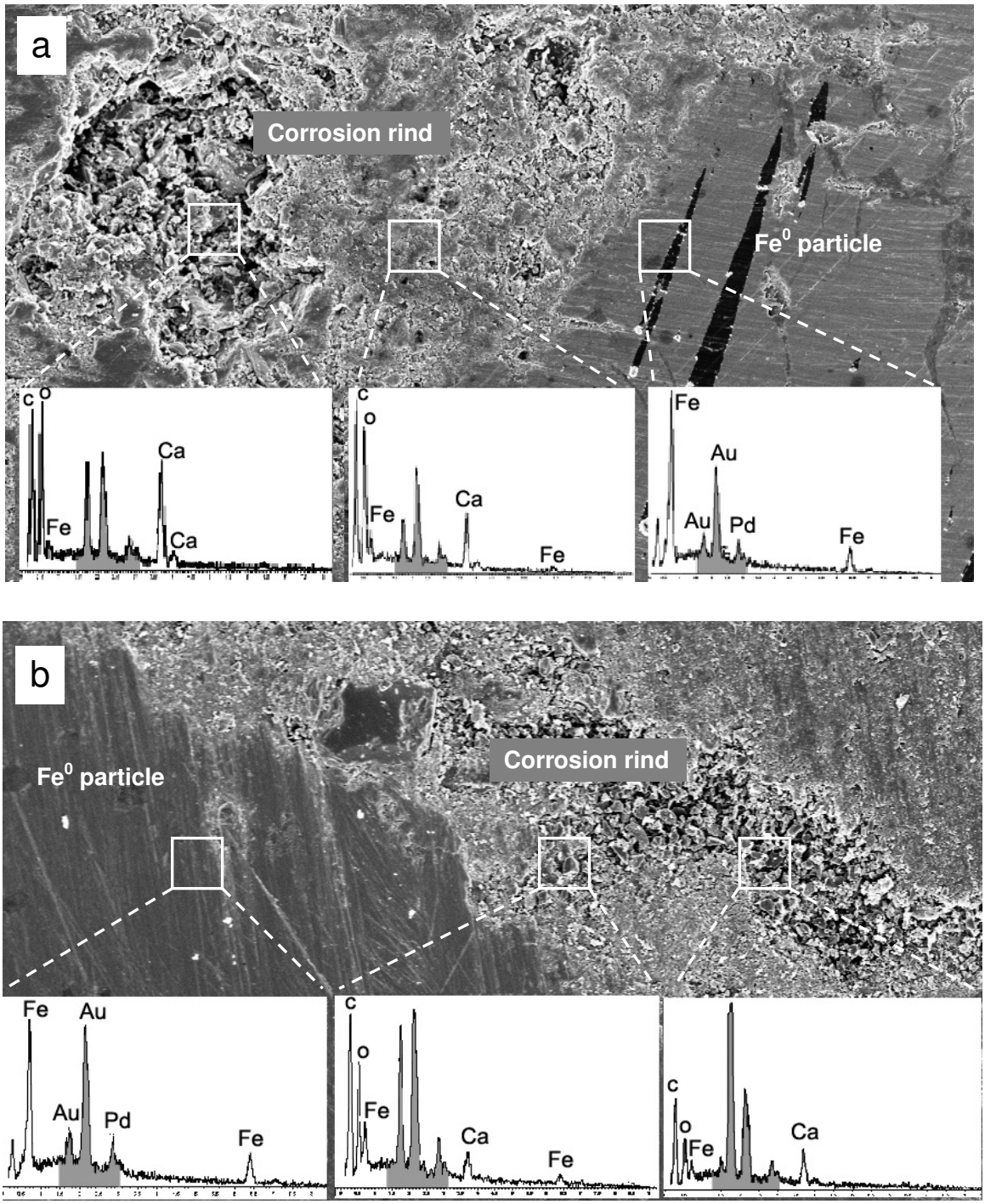

Figure 6. Additional cross section SEM images showing the EDX mapping of changes of elemental compositions across the corrosion rind surrounding ZVI particles.

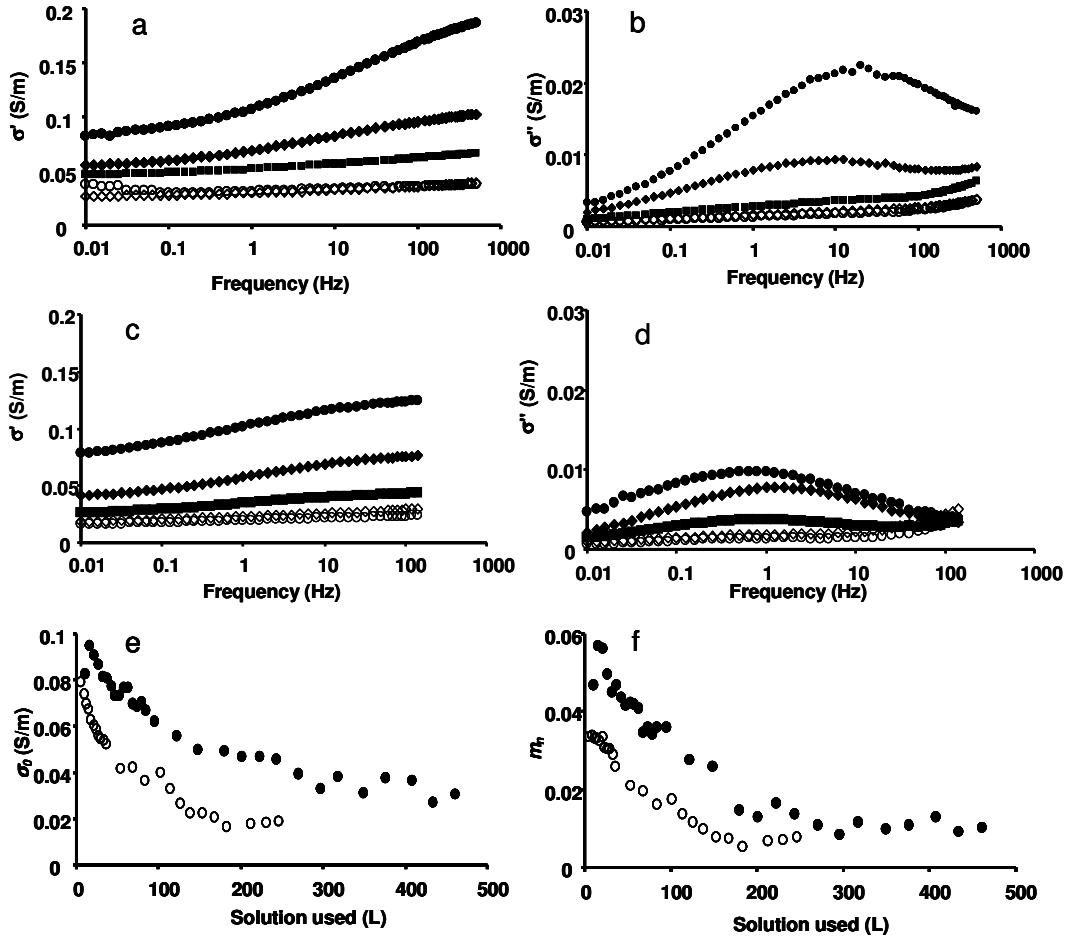

Figure 7. Spectral and model-fitted electrical data of the experiment. (a) σ' and (b) σ" of Helena column at channel 2 after various volumes of solution: 5L (●), 116L (♦), 217L (■), 312L (○), and 428L (◊);(c) σ' and (d) σ" of KC column at channel 2 after various volumes of solution: 3L (●), 65L (♦), 123L (■), 179L (○), and 242L (◊); Cole Cole model parameter (e) σ_0 and (f) m_n at channel 2 of Helena (●) and KC (○) columns as a function of solution usage. Note that high frequency data (>200, and >500 Hz for KC and Helena column, respectively) were discarded due to the high coupling noise.

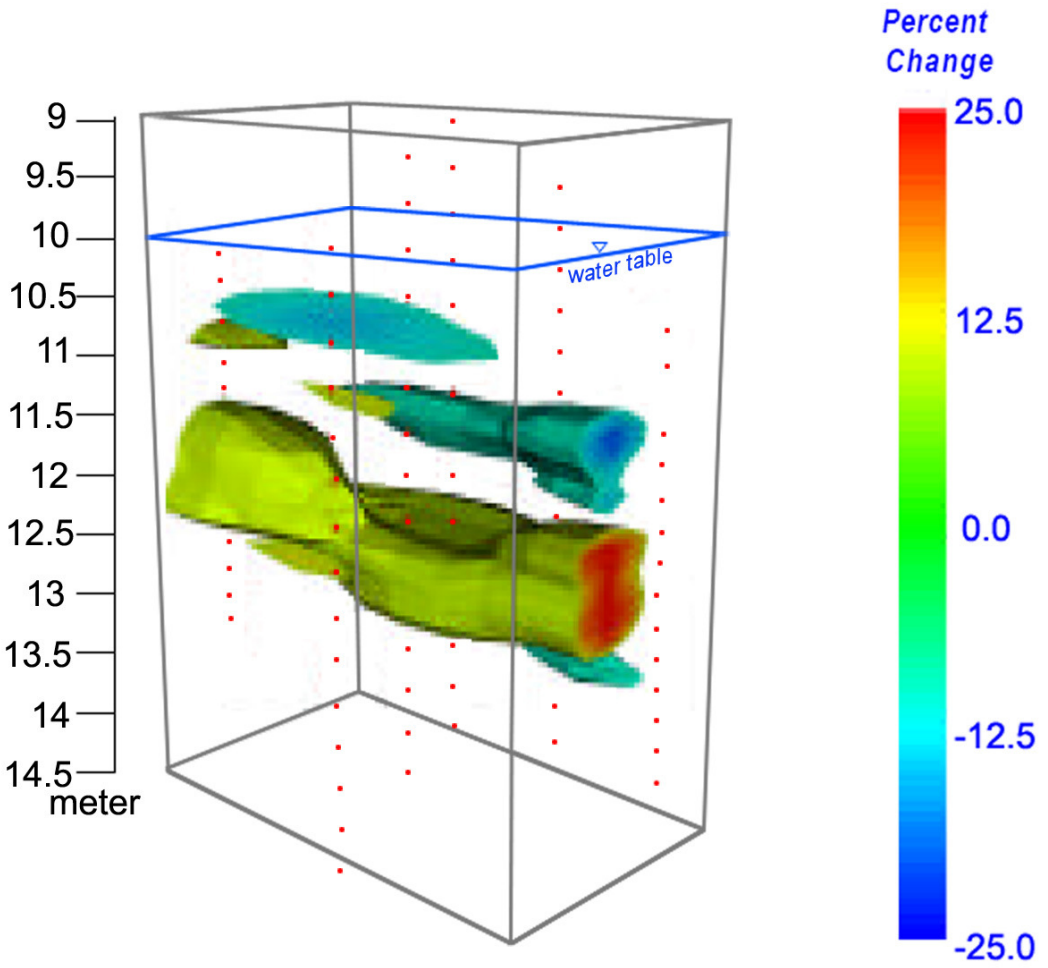

Figure 8. An ERT 3-D image of the Helena barrier plotted as the change in resistivity from a 1 Hz background image taken on December 2006 to Jun 2007. Red dots represent locations of electrodes and blue lines represent the location of water table.

Table 1. Saturation indices (SI) of potential precipitate mineral phases of interest calculated based on PHREEQC simulations.

Phases	SI of KC	SI of Helena
Aragonite	0.31	0.53
Calcite	0.49	0.71
Ferrihydrite	3.59	4.22
Goethite	6.29	6.92
Hematite	14.98	16.24
Lepidocrocite	5	6.04
Maghemite	7.18	8.43
Magnetite	20.93	23.83
Siderite	1	1.57

Table 2. Percentage of changes of electrical conductivity (σ_0) and polarization magnitude (m_n) for both columns for the duration of the experiment.

Paramete	Column	Ch2	Ch3	Ch4	Ch5	Ch6	Ch7
Decrease of σ_0	Helena	63%	74%	64%	63%	67%	68%
	KC	76%	82%	87%	81%	68%	63%
Decrease of m_n	Helena	79%	75%	83%	73%	72%	74%
	KC	77%	82%	88%	86%	75%	79%